The Astrophysical Journal, 994:70 (13pp), 2025 November 20 https://doi.org/10.3847/1538-4357/ae0cb7

Formation of Polyoxymethylenes in Extraterrestrial Ice Analogs of Formaldehyde Exposed to Ionizing Radiation

Qi'ang Gong[1], Xilin Bai[1], Jinghui Lu[2], Jiuzhong Yang[2], Yang Pan[2], Zhenrong Sun[1], Ralf I. Kaiser[3], and Tao Yang[1,4,5]
[1] State Key Laboratory of Precision Spectroscopy, East China Normal University, Shanghai 200062, People's Republic of China; tyang@lps.ecnu.edu.cn
[2] National Synchrotron Radiation Laboratory, University of Science and Technology of China, Hefei, Anhui 230029, People's Republic of China
[3] Department of Chemistry, University of Hawaii at Manoa, Honolulu, HI 96822, USA; ralfk@hawaii.edu
[4] Xinjiang Astronomical Observatory, Chinese Academy of Sciences, 150 Science 1-Street, Urumqi, Xinjiang 830011, People's Republic of China
[5] Collaborative Innovation Center of Extreme Optics, Shanxi University, Taiyuan, Shanxi 030006, People's Republic of China

Received 2025 April 1; revised 2025 September 22; accepted 2025 September 25; published 2025 November 14

Abstract

Polyoxymethylenes (POMs) have long been hypothesized as key organics in comets, as their decomposition products could account for the possible extended cometary formaldehyde (H_2CO) source. However, POMs (X–$(CH_2O)_n$–Y; $n > 2$) are hitherto unobserved in deep space, and their possible formation mechanisms have still remained elusive. Here, we report on the laboratory formation of formaldehyde oligomers (H–$(CH_2O)_n$–H; $n = 2-4$) within extraterrestrial ice analogs of formaldehyde exposed to energetic electrons simulating secondary electrons generated by galactic cosmic rays passing through ices. The potential identification of these short-chain-length POMs, such as methoxymethanol (CH_3OCH_2OH), (methoxymethoxy)methanol ($CH_3OCH_2OCH_2OH$), and (methoxymethoxymethoxy)methanol ($CH_3OCH_2OCH_2OCH_2OH$), is accomplished by utilizing the synchrotron vacuum ultraviolet photoionization reflectron time-of-flight mass spectrometry (SVUV-PI-ReTOF-MS) technique coupled with the temperature-programmed desorption method. A radical-induced formaldehyde polymerization mechanism is proposed to address the formation of POMs, with the competition between chain propagation and chain termination determining the chain length of the polymers and availability of reactive hydrogen atoms. The electron impact ionization of POMs as well as accompanied fragmentation of their cations are analyzed via a quadrupole mass spectrometer, with mass peaks compared with those collected by the Positive Ion Cluster Composition Analyzer instrument on board the Giotto spacecraft in the inner coma of comet 1P/Halley, and by the Ptolemy instrument on the comet 67P/Churyumov–Gerasimenko. Our findings might support the proposal that (small) POMs exist on comets and nominate hitherto unobserved POMs such as (methoxymethoxy)methanol ($CH_3OCH_2OCH_2OH$) and (methoxymethoxymethoxy)methanol ($CH_3OCH_2OCH_2OCH_2OH$) for future astronomical searches.

Unified Astronomy Thesaurus concepts: Astrochemistry (75); Laboratory astrophysics (2004); Mass spectrometry (2094); Comet volatiles (2162); Interstellar molecules (849); Surface ices (2117)

1. Introduction

Comets are widely believed to be repositories of the primitive materials that existed prior to the formation of our solar system. The composition of comets, especially the volatile complex organics and refractory organic solids, is of significant interest to the astronomical community (W. A. Schutte et al. 1993; G. D. Cody et al. 2011; F. Goesmann et al. 2015; I. P. Wright et al. 2015). Astronomical observations provide valuable insight into the formation and composition of the cometary coma, which is produced by the emission of volatiles and dust when the comet is approaching small heliocentric distances. The coma is composed mainly of water (H_2O), with trace molecules such as methane (CH_4), formaldehyde (H_2CO), hydrogen cyanide (HCN), and ammonia (NH_3) (K. Altwegg et al. 2017; D. Bockelée-Morvan & N. Biver 2017). The spatial distribution of the released volatiles, as observed spectroscopically, presents the variation in the abundances of different molecular species with respect to nucleocentric distance. By analyzing the spatial distribution, the production site of a given cometary species can be determined, while distribution features provide significant information about complex physical and chemical processes on comets. Observational studies of comets, conducted using the Atacama Large Millimeter/submillimeter Array (ALMA) and NASA's Infrared Telescope Facility, revealed a significantly extended distribution of formaldehyde in the coma. This suggests that formaldehyde is not solely produced by direct sublimation from the comet's surface but may also originate from the chemical fragmentation of higher-molecular-mass organic compounds (M. A. DiSanti et al. 2006; M. A. Cordiner et al. 2014; C. Ejeta et al. 2023).

The hypothesis that polyoxymethylenes (POMs) serve as a potential chemical precursor of formaldehyde has been debated for years (W. A. Schutte et al. 1993; H. Cottin et al. 2004; N. Fray et al. 2006). POMs and POM-like polymers are characterized by their repeating building blocks ($-CH_2O-$). Despite the lack of direct detection evidence for POMs on comets, it was suggested that the thermal emission feature near 10 μm (1000 cm^{-1}) from the infrared observations of several comets could be ascribed to POMs, with POMs, as a refractory material, being the major component of cometary dust (K. S. Krishna Swamy et al. 1989; V. Vanysek & N. C. Wickramasinghe 1999; G. D. Cody et al. 2011). The multiphase chemical model, which takes into account the thermal and photodegradation of solid POMs, reproduced nicely the observed formaldehyde density profiles in comet 1P/Halley, thus suggesting that POMs may be an extended source of formaldehyde and present on the surface of the comet nucleus (H. Cottin et al. 2001; H. Cottin et al. 2004). In the renowned ESA Rosetta mission, three mass spectrometers —Ptolemy, COSAC, and ROSINA-DFMS—analyzed the surface materials on the cometary nucleus and gaseous composition within the coma (F. Goesmann et al. 2015; M. Rubin et al. 2015; I. P. Wright et al. 2015; K. Altwegg et al. 2016). Mass peaks obtained by Ptolemy showed an apparently regular distribution pattern, indicating the possibility of the presence of polymers such as POMs or ice tholin (I. P. Wright et al. 2015). However, a comprehensive comparison of the data from Ptolemy and ROSINA-DFMS provided a distinct perspective. Utilizing the ROSINA-DFMS for its exceptional high-resolution capability ($m/\Delta m$ 9000 at m/z 28), the peak at m/z 91 can be accurately attributed to the molecular formula $C_7H_7^+$ rather than $C_3H_7O_3^+$, thus implying that this mass peak corresponds to a hydrocarbon ion instead of POM-trimer (K. Altwegg et al. 2017; N. Hänni et al. 2022). The fitting analysis of the COSAC mass spectra likewise revealed no conclusive evidence for the presence of POMs (F. Goesmann et al. 2015; M. Meringer et al. 2018; G. Leseigneur et al. 2022). Consequently, there is a lack of consensus among these studies regarding the composition of comets with respect to formaldehyde and POMs, requiring novel investigations including astronomical observation, experimental simulation, and theoretical modeling.

Previous ice simulation experiments suggested that formaldehyde acts as a crucial precursor in the formation of POMs (W. A. Schutte et al. 1993; F. Duvernay et al. 2014; T. Butscher et al. 2016; T. Butscher et al. 2019), adopting Fourier-transform infrared (FTIR) spectroscopy to infer molecular products. The formaldehyde ice irradiated by the vacuum ultraviolet (VUV) light was probed in the solid state at 10 K, revealing that an infrared absorption band near $1000\,\mathrm{cm}^{-1}$ related to the C–O stretching mode can be attributed to POMs. In addition to FTIR spectroscopy, quadrupole mass spectrometry (QMS) was also employed to obtain mass spectra of the products after sublimation, which were discriminated by fitting fragmentation patterns in the NIST database (T. Butscher et al. 2016). However, further understanding of POMs such as the size distribution and chain lengths is challenging due to the similarity in structures and functional groups, resulting in strong overlapping of absorption bands in the FTIR spectra and interfering mass fragments in the electron-impact mass spectra (A. M. Turner & R. I. Kaiser 2020). Unique laboratory experiments assisted by theoretical calculations have to be introduced to enhance the comprehension of POMs and elucidating their formation mechanism.

Here, we present a combined experimental and theoretical demonstration on the synthesis and detection of short-chain-length POMs in formaldehyde ice analogs exposed to energetic electrons mimicking those generated by galactic cosmic rays (M. J. Abplanalp et al. 2016; C. R. Arumainayagam et al. 2019; A. M. Turner et al. 2021). Exploiting the temperature-programmed desorption (TPD) technique, molecular species formed in the irradiated ices are interrogated via the state-of-the-art synchrotron vacuum ultraviolet photoionization reflectron time-of-flight mass spectrometry (SVUV-PI-ReTOF-MS; C. Zhu et al. 2022; J. H. Marks et al. 2024). Benefiting from the soft ionization and tunability of synchrotron vacuum ultraviolet (SVUV) radiation, we extract the appearance energies and photoionization efficiency (PIE) curves of fragments of these POMs and determine the structural isomer methoxymethanol by comparing with the reference curve. Conventional QMS data are also utilized to obtain mass fragmentation patterns of products and compared with the literature data, reinforcing the identification of POMs as X–$(CH_2O)_n$–Y ($n \geqslant 2$), where X or Y represents the hydrogen atom ($\dot{H}$), the formyl radical ($H\dot{C}O$), the hydroxymethyl radical ($\dot{C}H_2OH$), and so forth. Further, we present the geometry structures and adiabatic ionization energies of methoxymethanol (CH_3OCH_2OH), (methoxymethoxy)methanol ($CH_3OCH_2OCH_2OH$), and (methoxymethoxymethoxy)methanol ($CH_3OCH_2OCH_2OCH_2OH$) isomers through high-level quantum chemical calculations and eventually propose that radical-induced polymerization mechanisms likely play a crucial role in the formation of POMs. Our findings provide competitive evidence for structural information and reaction mechanism of POMs, supporting formaldehyde oligomers H–$(CH_2O)_n$–H as the potential leading composition of X–$(CH_2O)_n$–Y products in irradiated formaldehyde ices under conditions relevant to extraterrestrial environments.

2. Results

2.1. SVUV-PI-ReTOF-MS

To identify the products, we exploited first the SVUV-PI-ReTOF-MS technique at a photon energy of 11.00 eV during the TPD phase of the experiments (Figure 1). Considering POMs as a family of molecules with similar structures and chemical properties, we observed a regular pattern of incrementally increasing mass-to-charge ratios (m/z) in steps of 30 amu at 61, 91, and 121 in irradiated formaldehyde ice experiments. The odd mass ions with notable intensities are determined as fragments resulting from dissociative photoionization, with the chemical composition limited to the elements carbon, hydrogen, and oxygen. It can thus be inferred that the signals with a consistent increment of m/z 30 (CH_2O^+) may be attributed to the dissociative photoionization products from one of the subgroups of POMs with different n sizes (X–$(CH_2O)_n$–Y). The TPD profiles for these three m/z are shown in Figure 1, illustrating the variation in signal intensity as a function of temperature. As a control experiment, the nonirradiated blank experiment was conducted to demonstrate that the products were generated from the irradiation processes of formaldehyde ices. The TPD profile of m/z 61 reveals a broad peak at 260 K, corresponding to a sublimation event from 220 to 300 K. For m/z 91, the TPD profile exhibits a peak shifted to 270 K with a signal extending from 230 to 310 K. In addition, the signal at m/z 121 is observed in the higher temperature range from 240 to 320 K, peaking at about 280 K; this trend is consistent with the physical property that larger molecules exhibit higher sublimation temperatures (B. M. Jones & R. I. Kaiser 2013). It is essential to highlight that the phenomenon of molecular sublimation is a complex process influenced by various factors such as ice thickness, heating rate, and in particular, the intermolecular interactions that exhibit pronounced effects within the ice matrix (J. A. Noble et al. 2012).

The fragment ion signal at m/z 61 suggests the presence of a $C_2H_6O_2$ parent compound, even though prior studies have indicated that methoxymethanol and ethylene glycol ($HOCH_2CH_2OH$) sublimate at temperatures close to 160 K

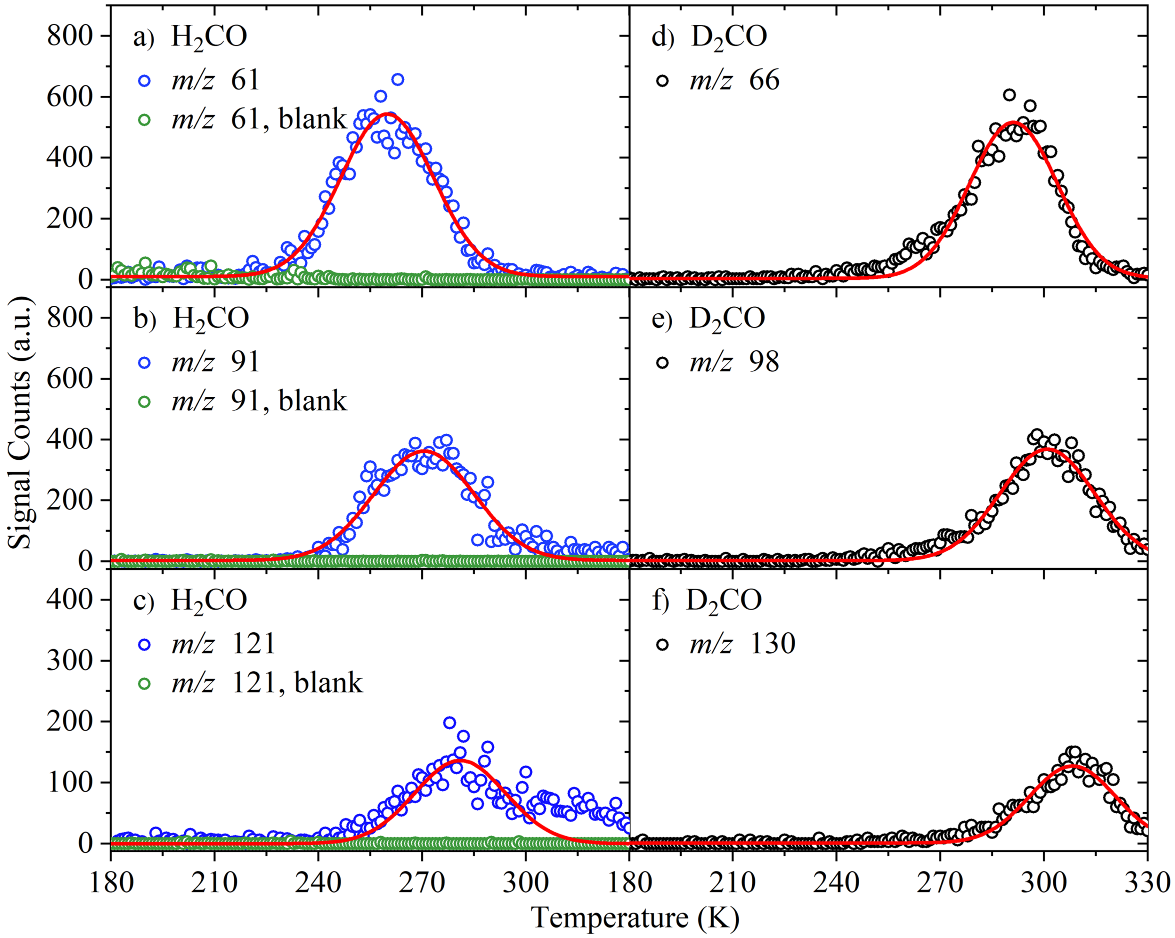

Figure 1. SVUV-PI-ReTOF-MS data recorded during the TPD phase of H_2CO ice (left) and D_2CO ice (right). The TPD profiles at (a) $C_2H_5O_2^+$ (m/z 61), (b) $C_3H_7O_3^+$ (m/z 91), (c) $C_4H_9O_4^+$ (m/z 121), (d) $C_2D_5O_2^+$ (m/z 66), (e) $C_3D_7O_3^+$ (m/z 98), and (f) $C_4D_9O_4^+$ (m/z 130) were obtained by exploiting the ReTOF spectrometer at a photon energy of 11.00 eV. The product signals from the irradiated H_2CO experiment (15 nA, 10 minutes; blue circles) were compared with the blank experiment (no irradiation; green circles) and irradiated D_2CO experiment (15 nA, 10 minutes; black circles). The data are fitted with Gaussian peaks (red lines).

and 200 K, respectively (C. Zhu et al. 2019; J. He et al. 2022). In our experiment, the elevated sublimation temperatures of products can be attributed to the substantial production of larger POM chains, which are nonvolatile and inhibit the lower temperature sublimation of other molecules. These molecules remain in the polymer matrix, trapped until larger POM chains undergo sublimation or thermal decomposition, exhibiting a characteristic codesorption behavior (T. Butscher et al. 2019). We also conducted the isotopic experiment exploiting formaldehyde-d2 (D_2CO) under the same conditions in order to investigate the elemental composition of three distinct ions. In the irradiated formaldehyde-d2 experiment, TPD signals at m/z 61 shifts by 5 amu to m/z 66, as shown in Figure 1(d), indicating that the ion contains five hydrogen atoms and thus corresponds to the chemical formula with $C_2H_5O_2^+$ rather than $C_3H_9O^+$. Similarly, the signals at m/z 91 and 121 are shifted by 7 and 9 amu, respectively (Figures 1(e) and (f)), which confirm the chemical formulae of products in the irradiated formaldehyde ices as $C_3H_7O_3^+$ and $C_4H_9O_4^+$. Additionally, the sublimation temperatures of all deuterated products increase by typically 30 K due to their higher molecular weight.

2.2. PIE Curves

It is now evident that POMs with similar structures are produced during the irradiation of formaldehyde, whose fragments depict molecular formulae of $C_2H_5O_2^+$, $C_3H_7O_3^+$, and $C_4H_9O_4^+$ at m/z 61, 91, and 121, respectively. The structural identification of the smallest member, corresponding to the signal at m/z 61, is important because it provides a reliable foundation for determining the structure of a long-chain POM. However, it is challenging to trace back the origin of the fragment ions because diverse parent cations can yield identical or similar fragment ions. For instance, multiple fragments can be generated through dissociative photoionization of ethylene glycol ($HOCH_2CH_2OH$) including $C_2H_5O_2^+$ with an appearance energy of 10.84 eV (H. Wang et al. 2022). Additionally, compelling evidence has been provided for the detection of the resonance-stabilized fragment ion, hydroxymethoxymethylium ($CH_3OCH(OH)^+$) formed through a dissociation channel involving the loss of a methyl radical ($\dot{C}H_3$) from the 1-methoxyethanol cation ($CH_3OCH(OH)CH_3^+$) (J. Wang et al. 2023). In recent studies, $CH_3OCH(OH)^+$ has also been identified as the primary product of the photoionization process of methoxymethanol, and its appearance energy was determined to be 10.24 ± 0.05 eV (N. A. Hansen et al. 2024). The absence of the expected parent cation signals in the experiments indicated a pronounced preference in the production of the $CH_3OCH(OH)^+$ fragment ion.

To facilitate the identification of POMs, the PIE curve fitting method was employed. The PIE curve—either of the molecular parent ion or fragment ions—reports the ion yield as a function of photon energy, offering vital information such

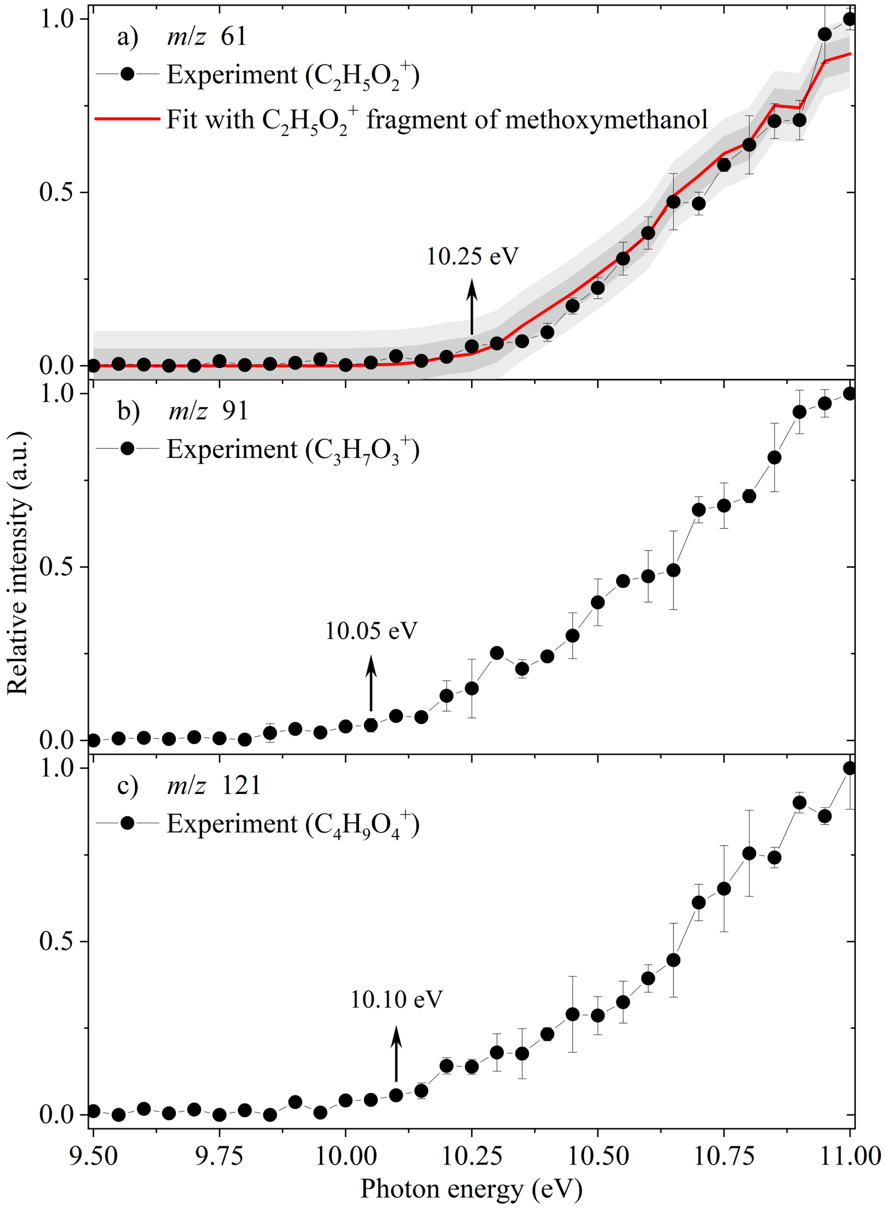

Figure 2. Experimental and reference PIE curves recorded at (a) *m/z* 61, (b) *m/z* 91, and (c) *m/z* 121. The black circles denote the experimental PIE curves, while the red line indicates the fitted reference PIE curve for the $C_2H_5O_2^+$ fragment of methoxymethanol. The dark gray and light gray shaded regions represent the 5% and 10% uncertainties from the reference PIE curve, respectively, while the error bars represent the experimental uncertainties (1σ).

as the ionization energy of the parent molecule and/or the appearance energy of fragment(s). Serving as a molecular fingerprint, the PIE curve further provides insights into distinct molecular structures (structural isomers), thus establishing its significance as a versatile and valuable analytical tool in the fields of combustion, catalysis, and astrochemistry (Y. Li & F. Qi 2010; F. Qi 2013; O. Kostko et al. 2016; R. Komorek et al. 2018; Z. Zhou et al. 2022; C. Zhu et al. 2022). The PIE scanning was conducted within the appropriate temperature range, where considerable molecular sublimation events were observed. During the TPD phase, the SVUV photon energy was finely tuned from 9.50 to 11.00 eV in a 0.05 eV increment to record the signal counts for *m/z* 61, 91, and 121. The PIE curves were obtained by normalizing the counts to the intensity at a corresponding temperature and to photon flux yields, with the intensity being derived from the Gaussian peak fitting of the TPD profiles. As illustrated in Figure 2(a), the experimentally obtained PIE curve of *m/z* 61 indicating the appearance energy of 10.25 ± 0.05 eV can fit well with the reference PIE curve of the $C_2H_5O_2^+$ fragment of methoxymethanol (N. A. Hansen et al. 2024). To the best of our knowledge, there are currently no experimental studies concerning $CH_3OCH_2OCH_2OH$ and POMs with higher polymerization degrees; thus, there is a lack of known reference PIE curves for fitting purposes.

It is therefore intriguing to elucidate the origin of fragment ions $C_2H_5O_2^+$, $C_3H_7O_3^+$, and $C_4H_9O_4^+$. Once formed in the irradiation of formaldehyde, the subliming POMs will be initially photoionized by SVUV photons in the energy range examined. The calculated ionization energies of the three most stable conformers of H–$(CH_2O)_n$–H ($n = 2$–4) at the CCSD(T)/CBS//B3LYP/cc-pVTZ level of theory are determined to be 9.94–10.11 eV ($CH_3OCH_2OH^+$, *m/z* 62), 9.70–10.07 eV ($CH_3OCH_2OCH_2OH^+$, *m/z* 92), and 9.76–9.83 eV ($CH_3OCH_2OCH_2OCH_2OH^+$, *m/z* 122),

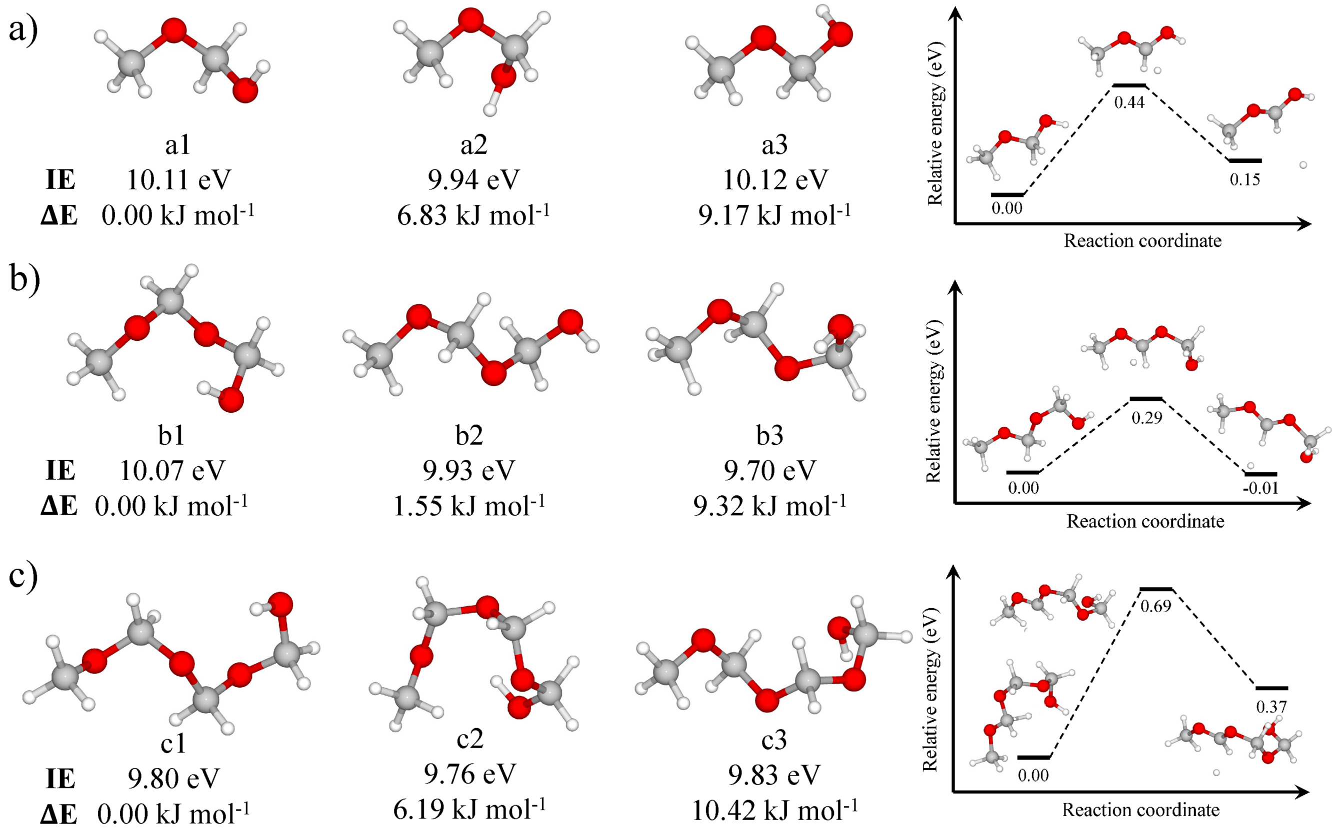

Figure 3. Adiabatic ionization energies (IEs) and relative energies (ΔEs) of (a) methoxymethanol (CH_3OCH_2OH), (b) (methoxymethoxy)methanol ($CH_3OCH_2OCH_2OH$), and (c) (methoxymethoxymethoxy)methanol ($CH_3OCH_2OCH_2OCH_2OH$) calculated at the CCSD(T)/CBS//B3LYP/cc-pVTZ level of theory, as well as their potential energy surfaces involving the associated dissociative channels into the hydrogen-loss fragment ions.

respectively (Figure 3). However, no such parent cations were observed in the energy range of 9.5 and 11.0 eV, but their fragment ions yielded signals at m/z 61 ($C_2H_5O_2^+$), 91 ($C_3H_7O_3^+$), and 121 ($C_4H_9O_4^+$). The computed dissociation barriers of 0.44, 0.29, and 0.69 eV with respect to the atomic hydrogen loss of the parent cations shall hinder the observation of fragment ions at the experimentally derived onsets of 10.25 ± 0.05 eV ($C_2H_5O_2^+$), 10.05 ± 0.05 eV ($C_3H_7O_3^+$), and 10.10 ± 0.05 eV ($C_4H_9O_4^+$). How can this apparent "discrepancy" be explained?

Let us consider the photoionization and fragmentation of methoxymethanol as a benchmark first. The range of ionization energies for methoxymethanol of 9.94–10.11 eV plus the barrier for the atomic hydrogen loss of 0.44 eV suggests that the signal at m/z 61 should appear at 10.38–10.55 eV. However, N. A. Hansen et al. (2024) proposed that the atomic hydrogen de facto is ejected "barrierlessly" through the tunneling effect; solely the reaction energy of 0.15 eV has to be accounted for the dissociation of the methoxymethanol cation (Figure 3(a)). Consequently, the signal at m/z 61 is expected to commence at 10.09–10.26 eV. Our experimental photoionization onset of 10.25 ± 0.05 eV ($C_2H_5O_2^+$) along with the PIE curve of m/z 61 fully supports the involvement of tunneling, thus benchmarking the methoxymethanol system and its fragment at m/z 61.

We are translating this framework of tunneling now to (methoxymethoxy)methanol ($CH_3OCH_2OCH_2OH$) and the parent cation ($C_3H_8O_3^+$, m/z 92) with ionization energies of 9.70–10.07 eV (Figure 3(b)). Adding the barrier of the atomic hydrogen loss of the cation at m/z 92 would expect the signal of m/z 91 to show up at 9.99–10.36 eV, while eliminating this barrier due to tunneling and accounting for the reaction energy of the atomic hydrogen loss should yield the signal at m/z 91 from 9.69 to 10.06 eV on. In this case, the experimentally observed onset of 10.05 ± 0.05 eV for m/z 91 can account for the existence of a barrier but also for the involvement of tunneling in the atomic hydrogen loss. For the (methoxymethoxymethoxy)methanol ($CH_3OCH_2OCH_2OCH_2OH$) and its parent cation ($C_4H_{10}O_4^+$, m/z 122), the range of ionization energies of 9.76–9.83 eV shall result in appearance energies of 10.45–10.52 eV for $C_4H_9O_4^+$ (m/z 121) by taking into account of the barrier for the atomic hydrogen loss (Figure 3(c)). But with a dominating tunneling mechanism, the appearance energy for m/z 121 is lowered to only 10.13–10.20 eV, which agrees with the experimental onset of 10.10 ± 0.05 eV for m/z 121. Overall, the tunneling-mediated, predicted appearance energies of 10.09–10.26 eV, 9.69–10.06 eV, and 10.13–10.20 eV match well with the experimentally observed onsets of 10.25 ± 0.05 eV ($C_2H_5O_2^+$), 10.05 ± 0.05 eV ($C_3H_7O_3^+$), and 10.10 ± 0.05 eV ($C_4H_9O_4^+$), respectively.

2.3. Electron-impact Mass Spectra

The electron-impact mass spectra recorded during the TPD phase were analyzed to further strengthen the identification of the products. It shall be stressed that the quadrupole mass spectrometer utilizes 70 eV electrons to ionize neutral molecules, thus yielding a greater variety of fragment ions. As shown in Figure 4, ions related to the POM fragmentation pattern were detected at m/z 31, 45, 47, 61, 75, 77, 91, 105,

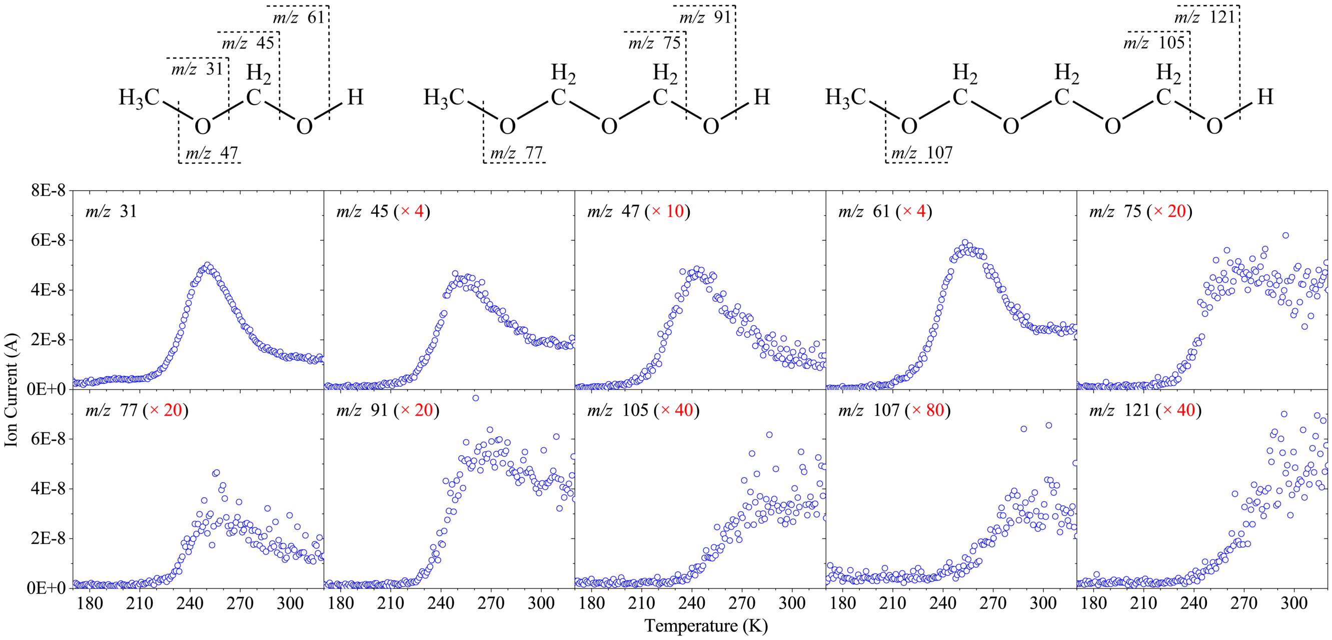

Figure 4. POM fragmentation patterns for $\mathrm{CH_3OCH_2OH}$, $\mathrm{CH_3OCH_2OCH_2OH}$, and $\mathrm{CH_3OCH_2OCH_2OCH_2OH}$ (top); QMS data recorded during the TPD phase of the irradiated $\mathrm{H_2CO}$ ices (bottom). Numbers in parentheses represent the multiplication factors of ion signal intensities.

107, and 121, which displays a periodic increment regularity with repeating mass intervals of 14 and 16. The similarity in the temperature ranges at which the product sublimation events occur, as compared with the TPD profiles obtained by the SVUV-PI-ReTOF-MS method, suggests a high degree of reliability and validity in the results. In particular, ions of m/z 31, 45, and 61 have been proven to be significant mass spectral fragments indicative of $\mathrm{CH_3OCH_2OH}$ (R. A. Johnson & A. E. Stanley 1991; T. D. Harris et al. 1995; H. Schneider et al. 2019; J. He et al. 2022). Note that in prior irradiated formaldehyde experiments, the existence of POMs was identified by the electron-impact mass spectra through its characteristic fragments at m/z 47 and 61, and the hypothesized structure of POMs was proposed to be $\mathrm{X{-}(CH_2O)}_n\mathrm{{-}Y}$ (T. Butscher et al. 2016, 2019). Therefore, based on our QMS characteristic fragmentation mass spectra alone, we can assign our POMs ($\mathrm{X{-}(CH_2O)}_n\mathrm{{-}Y}$ ($n \geqslant 2$; X or Y = $\dot{\mathrm{H}}$, $\mathrm{H\dot{C}O}$, $\dot{\mathrm{C}}\mathrm{H_2OH}$, etc.)) as the predominant products in our irradiated formaldehyde ices.

3. Proposed Reaction Mechanisms

We aim to propose the reaction mechanisms by combining our findings with prior experimental and theoretical insights. Utilizing cryogenic matrices and infrared spectroscopy, the generation of $\mathrm{H\dot{C}O}$ and $\dot{\mathrm{C}}\mathrm{H_2OH}$ was identified after VUV irradiation and matrix annealing process on formaldehyde ice (T. Butscher et al. 2017; T. Butscher et al. 2019). These radicals were also observed as degradation products of methanol ($\mathrm{CH_3OH}$) (C. J. Bennett & R. I. Kaiser 2007; C. J. Bennett et al. 2007; S. Maity et al. 2015; N. F. Kleimeier et al. 2021) and reaction products of suprathermal hydrogen atoms with carbon monoxide (S. Maity et al. 2015; K. J. Chuang et al. 2016). Here, the formation of $\mathrm{H\dot{C}O}$ and $\dot{\mathrm{H}}$ is triggered by breaking the carbon–hydrogen bond within the formaldehyde molecule (Reaction (1)). Given the ubiquity of hydrogenation reactions in unsaturated ice molecules such as the sequential hydrogenation of carbon monoxide (N. Watanabe et al. 2004; K. J. Chuang et al. 2016), suprathermal hydrogen atoms with kinetic energies of a few eV can overcome the barrier of addition to the carbon–oxygen double bond of the formaldehyde molecule, leading to the formation of $\dot{\mathrm{C}}\mathrm{H_2OH}$ (Reaction (2)). It shall not be omitted that the hydrogenation of formaldehyde may also lead to the possible formation of the methoxy radical ($\mathrm{CH_3\dot{O}}$). This radical, which is believed to play a significant role in the formation of complex organic molecules in the interstellar medium, has been discovered toward the cold dark cloud B1-b (J. Cernicharo et al. 2012). However, the $\dot{\mathrm{H}}$-addition to $\mathrm{H_2CO}$ could proceed preferentially through $\dot{\mathrm{C}}\mathrm{H_2OH}$ rather than $\mathrm{CH_3\dot{O}}$ in the pure formaldehyde (T. Butscher et al. 2016; T. Butscher et al. 2019; Y. Layssac et al. 2020). The $\mathrm{CH_3\dot{O}}$ radical could isomerize to $\dot{\mathrm{C}}\mathrm{H_2OH}$ through intramolecular hydrogen atom transfer (M. Iwasaki & K. Toriyama 1978; K. Toriyama & M. Iwasaki 1979; H. Tachikawa 1993), and the nondetection of methyl formate ($\mathrm{CH_3OCHO}$) also implies that $\mathrm{CH_3\dot{O}}$ is not efficiently formed in our irradiated formaldehyde ices:

$$\mathrm{H_2CO} \rightarrow \mathrm{H\dot{C}O} + \dot{\mathrm{H}} \tag{1}$$

$$\mathrm{H_2CO} + \dot{\mathrm{H}} \rightarrow \dot{\mathrm{C}}\mathrm{H_2OH}. \tag{2}$$

Here, a radical-induced polymerization mechanism is suggested to untangle the formation process of POMs. The $\dot{\mathrm{C}}\mathrm{H_2OH}$ radical may initiate a reaction with one of the neighboring $\mathrm{H_2CO}$ molecules to generate the $\dot{\mathrm{C}}\mathrm{H_2OCH_2OH}$ radical (Reaction (3)). We shall emphasize that under thermal conditions, this reaction has a barrier of 0.62 eV (T. Butscher et al. 2019). However, since the $\dot{\mathrm{C}}\mathrm{H_2OH}$ radical is formed via Reaction (2) with a suprathermal hydrogen atom, the $\dot{\mathrm{C}}\mathrm{H_2OH}$ radical is then highly vibrationally excited; this internal energy can be used to overcome the barrier of suprathermal hydrogen addition to the carbon–oxygen double bond of the neighboring $\mathrm{H_2CO}$ molecule. Since abundant suprathermal hydrogen atoms are generated upon irradiation and exhibit strong mobility at

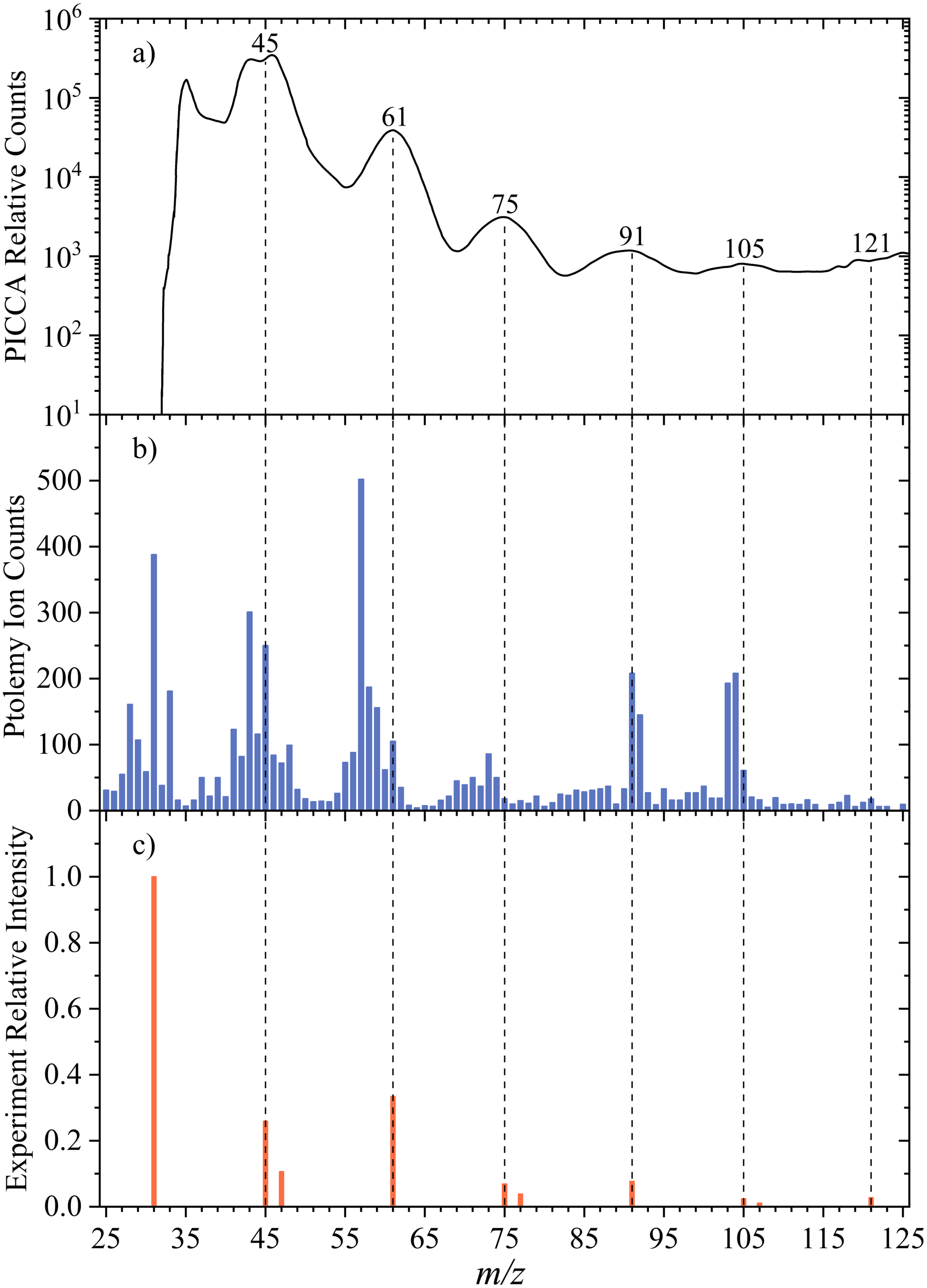

Figure 5. Comparison of experimental and observed mass spectra for POMs. (a) PICCA spectra. (b) Ptolemy spectra. (c) Integrated mass spectra of POMs in the 180 −320 K temperature range derived from TPD profiles measured by QMS.

low temperatures due to diffusion (B. Senevirathne et al. 2017), they should play a significant role in chain termination compared with $\dot{C}H_2OH$. This can be warranted by the absence of ethylene glycol ($HOCH_2CH_2OH$) in our experiments, given that its formation preferentially occurs via $\dot{C}H_2OH$ recombination (V. M. Rivilla et al. 2017) compared to the chain termination of $\dot{C}H_2OH$ to the $\dot{C}H_2OCH_2OH$ radical, which can be formed via the addition of $\dot{C}H_2OH$ to H_2CO. Thereafter, the reaction proceeds through two competing pathways, i.e., the chain propagation involving the continuation of reaction with an additional H_2CO molecule and the chain termination through addition of $\dot{H}$ to the radical center of $\dot{C}H_2OCH_2OH$ (Reaction (4)) forming CH_3OCH_2OH:

$$\dot{C}H_2OH + H_2CO \rightarrow \dot{C}H_2OCH_2OH \quad (3)$$

$$\dot{C}H_2OCH_2OH + \dot{H} \rightarrow CH_3OCH_2OH. \quad (4)$$

Similar processes may contribute to the formation of longer-chain molecules, such as $CH_3OCH_2OCH_2OH$ and $CH_3OCH_2OCH_2OCH_2OH$. It is plausible that the $H\dot{C}O$ radical could also initiate or terminate polymerization reaction. However, the corresponding reaction products glycolaldehyde ($HOCH_2CHO$) and methyl formate were not identified in our experiments, potentially due to their negligible production at the low irradiation dose. In addition, the dimerization of $H\dot{C}O$ should tend to form carbon monoxide (CO) and H_2CO rather than glyoxal (CHOCHO) (T. Butscher et al. 2017), while the $H\dot{C}O$ can dissociate to CO and $\dot{H}$ via a barrier of 0.78 eV (J. S. Francisco et al. 1988). Indeed, our electron-impact mass spectra at m/z of 28 revealed two distinct TPD profiles, and the CO desorption peaking at 20 K is so strong that it is comparable to that of H_2CO (Figure A1). The $\dot{C}H_2OH$ radical may be more favored for polymerization reaction than $H\dot{C}O$, a notion that has also been supported by prior experimental and theoretical studies (T. Butscher et al. 2019). Therefore, we conclude that formaldehyde oligomers $H–(CH_2O)_n–H$ likely constitute the dominant components of POMs ($X–(CH_2O)_n–Y$; $n \geqslant 2$, X or Y = $\dot{H}$, $H\dot{C}O$, $\dot{C}H_2OH$, etc.) under our experimental conditions.

4. Astrophysical Implications

Methoxymethanol was first discovered using the ALMA toward the high-mass star-forming region NGC 6344I (B. A. McGuire et al. 2017). Several laboratory studies have revealed that methanol ice is a vital precursor to methoxymethanol. Exposure of the methanol ice analog to photons or electrons leads to the formation of $CH_3\dot{O}$ and $\dot{C}H_2OH$ radicals followed by radical–radical recombination to generate methoxymethanol along with its isomers $HOCH_2CH_2OH$ and CH_3OOCH_3 (K. K. Sullivan et al. 2016; H. Schneider et al. 2019; C. Zhu et al. 2019; F. Schmidt et al. 2021). However, the chemical kinetics model, which exclusively contains the reaction pathways about the combination of $CH_3\dot{O}$ and $\dot{C}H_2OH$, produces an unexpectedly low amount of CH_3OCH_2OH. The calculated abundance ratio of CH_3OCH_2OH to CH_3OH ($\sim 10^{-7}$) is markedly lower than the observationally derived value (1:34) (B. A. McGuire et al. 2017), implying the presence of additional formation pathways for CH_3OCH_2OH. Consequently, our research suggests that the synthesis of CH_3OCH_2OH in the interstellar medium might be associated with the formaldehyde polymerization mechanism.

From the perspective of interstellar exploration, our results are crucial for interpreting the complicated observational data of comets as well. When the Positive Ion Cluster Composition Analyzer (PICCA) instrument on the Giotto spacecraft conducted measurements of the inner coma of comet 1P/Halley, the detected mass spectra exhibited a regular pattern of mass peaks, which were tentatively attributed to the short polymer chains of POMs (W. F. Huebner 1987; W. F. Huebner et al. 1989). Although the Ptolemy instrument provided potential evidence for POMs on comet 67P/Churyumov–Gerasimenko (I. P. Wright et al. 2015), their presence has been challenged due to the lack of reference experimental data for short-chain POMs (K. Altwegg et al. 2017; T. Butscher et al. 2019). In this study, we compared the mass peaks detected in our QMS for POMs with those reported by PICCA and Ptolemy (Figure 5), demonstrating consistency in terms of mass distribution. Our findings support the proposal that (small) POMs may exist on cometary nuclei, likely formed through formaldehyde polymerization. It is important to note that Ptolemy analyzed numerous cometary species (K. Altwegg et al. 2017); our experiment only includes three POM molecules, and their concentration ratios vary dramatically with the radiation dose. Thus, it is still challenging to fully match Ptolemy's results in terms of the signal intensity. Furthermore, the fragmentation patterns of 16 candidate cometary compounds were used to fit the COSAC mass spectrum, applying an Occam's razor approach or more rigorous statistical methods (F. Goesmann et al. 2015; M. Meringer et al. 2018). Subsequently, through nonnegative least quares fitting and Monte Carlo simulations, the 12 most probable molecules were screened from the NIST mass spectra database of 120 compounds, with no POMs included (G. Leseigneur et al. 2022). Nevertheless, due to the lack of suitable candidate molecules in the NIST database contributing to the m/z 61 signal, discrepancies persist between the fitted spectrum and the original COSAC data. Our study suggests that CH_3OCH_2OH could be considered as a potential additional candidate, which may lead to a more accurate interpretation of the observed mass spectra (N. Hänni et al. 2023). In addition, it is suggested that formaldehyde oligomers are volatile. The TPD phase in the experiment simulates the gradual warming process of cometary surfaces, sublimating the frozen molecules into the gas phase. Therefore, it is reasonable to anticipate that formaldehyde oligomers, such as $CH_3OCH_2OCH_2OH$ and $CH_3OCH_2OCH_2OCH_2OH$, which have been unobserved hitherto, are likely to be discovered using large radio telescopes such as ALMA. Their unambiguous identification may conclusively resolve the long-standing debate regarding the presence of POMs on comets.

Acknowledgments

The work was conducted under a Memorandum of Understanding (MOU) between the East China Normal University (ECNU), the University of Hawaii at Manoa (UHM), and the National Synchrotron Radiation Laboratory (NSRL) at the University of Science and Technology of China (USTC). The ECNU team acknowledges the support from the National Natural Science Foundation of China (12034008, 12250003, 92461301, and 12274140), the Xinjiang Tianchi Talent Program (2023), the Natural Science Foundation of Shanghai (22ZR1421400), and the Program for Professor of Special Appointment (Eastern Scholar) at Shanghai Institutions of Higher Learning. R.I.K. acknowledges the support from the US National Science Foundation (NSF) (AST 2403867).

Conflict of Interest

The authors declare no conflict of interest.

Appendix

A.1 Experimental Methods

Experiments were conducted at the Shanghai–Hawaii–Hefei Advanced Research Center, which innovatively applied the SVUV-PI-ReTOF-MS to astrochemistry simulation experiments, utilizing the VUV beamline BL03U at the National Synchrotron Radiation Laboratory. This machine consists of an ultrahigh vacuum chamber that has been evacuated to a few 10^{-10} Torr. Within the chamber, a polished silver substrate ($12.6 \times 15.1\ \mathrm{mm}^2$), which is interfaced to a cold head and cooled to 4.8 ± 0.1 K by a closed cycle helium refrigerator (Sumitomo Heavy Industries, RDK-415E), serves as a platform for the deposition of samples. The gas-phase monomer H_2CO or D_2CO was prepared by heating the paraformaldehyde ($(CH_2O)_n$; 95%; Aladdin Scientific Corp.) and paraformaldehyde-d2 ($(CD_2O)_n$; 98 atom% D; Sigma-Aldrich) to about 70°C. The gaseous sample was subsequently deposited onto the silver surface through a glass capillary array (main chamber pressure at 2×10^{-8} Torr) to produce solid H_2CO or D_2CO ice, and the ice thickness was characterized by counting the number of fringes via laser interferometry with a helium–neon (He–Ne) laser (Melles-Griot, 25-LHP-230, 632.8 nm) (J. B. Bossa et al. 2012; A. M. Turner et al. 2015). Employing the interference equation calculation with the refractive index parameter of n_{CH2O} at 1.33 ± 0.04 and the number of fringes as 3, the thickness of the formaldehyde ice was determined to be 710 ± 20 nm (M. Bouilloud et al. 2015).

After deposition, the substrate was repositioned to allow the surface ice materials to be irradiated with high-energy electrons. The irradiation procedure employed 5 keV electrons at a current of 15 ± 1 nA for 10 minutes (SPECS GmbH, EQ 22/35 electron source), with an incident angle of 70° relative to surface normal of the substrate. The interaction between the electron beam and the solid materials was simulated using CASINO 2.42 software (D. Drouin et al. 2007). The simulation results (Table A1) indicated that the average penetration depth of the electrons was 360 ± 40 nm and the irradiation dose was 0.41 ± 0.06 eV per H_2CO molecule (M. Förstel et al. 2016).

Following irradiation, the TPD was conducted by heating the substrate from 5 to 320 K at a rate of $1\ \mathrm{K\ minute}^{-1}$. The substrate temperature was monitored by a cryogenic temperature sensor (Lake Shore, DT-470) and controlled using a resistive heater, which was regulated by a programmable temperature controller (Lake Shore, Model 336). During the TPD phase, SVUV light was applied to selectively ionize the subliming molecules, and the resulting cations were then resolved at a specific m/z and detected by microchannel plates (MCPs) within the ReTOF mass spectrometer (Jordan TOF Products). Controlled by a pulse delay generator (Quantum Composers, 9528) at a repetition rate of 15 kHz, the timing between the extraction grid voltage of the ReTOF and the multichannel scaler (Fast ComTec, P7889) were optimized such that the optimum signal-to-noise ratio was achieved. The signal generated upon the detection of ions on the MCPs was subsequently amplified using a preamplifier (Ortec, 9306), discriminated by an F-100TD amplifier-discriminator (Advanced Research Instruments Corp.), and ultimately recorded by the multichannel scaler with a resolution of 3.2 ns. In addition to the SVUV-PI-ReTOF-MS technique, a quadrupole mass spectrometer (Pfeiffer Vacuum, PrismaPlus QMG220) equipped with a secondary electron multiplier was also utilized to monitor the subliming molecules (Figure A1).

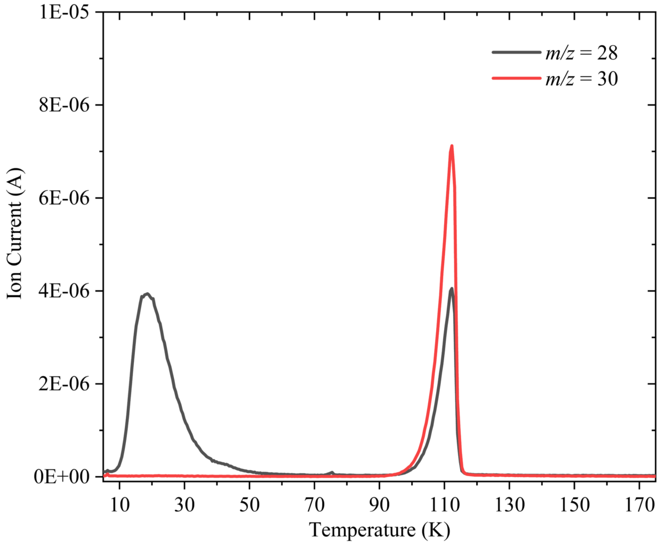

Figure A1. QMS data recorded during the TPD phase of the irradiated H_2CO ice at m/z of 28 (black line) and 30 (red line), respectively.

Table A1
Data Used to Calculate the Average Dose per Molecule within the Irradiated Ice

Parameter	H_2CO
Irradiation current, I (nA)	15 ± 1
Initial kinetic energy of the electrons, E_{init} (keV)	5
Total number of electrons	$(3.4 \pm 0.2) \times 10^{14}$
Average penetration depth, l (nm)[a]	360 ± 40
Average kinetic energy of backscattered electrons, E_{bs} (keV)[a]	3.3 ± 0.3
Fraction of backscattered electrons, f_{bs}[a]	0.357 ± 0.036
Average kinetic energy of transmitted electrons, E_{trans} (keV)[a]	1.0 ± 0.1
Fraction of transmitted electrons, f_{trans}[a]	0.007 ± 0.001
Density of the ice, ρ (g cm^{-3})	0.81 ± 0.03
Irradiated area, A (cm^2)	0.9
Total molecules processed	$(5.3 \pm 0.7) \times 10^{7}$
Dose per molecule (eV)	0.41 ± 0.06

Note.
[a] Output values from CASINO simulations.

A.2 Theoretical Methods

The adiabatic ionization energies of POMs (H–$(CH_2O)_n$–H; $n = 2-4$; Figure 3) were calculated at the CCSD(T)/CBS//B3LYP/cc-pVTZ level of theory, with the obtained structure and ionization energy of CH_3OCH_2OH being consistent with previous research (R. A. Motiyenko et al. 2018; N. A. Hansen et al. 2024; D. Missaoui et al. 2024). Geometry optimization and frequency analysis of all molecular structures in the neutral and cationic states were performed employing the hybrid density functional theory B3LYP (C. Lee et al. 1988; A. D. Becke 1993) with the cc-pVTZ basis set (T. H. Dunning 1989; R. A. Kendall et al. 1992). Based on optimized structures, coupled cluster theory CCSD(T) (G. D. Purvis, III. & R. J. Bartlett 1982; R. J. Bartlett & M. Musiał 2007) with both the cc-pVDZ and cc-pVTZ basis sets was employed to

Table A2

Optimized Cartesian Coordinates (Å), Vibrational Frequencies (cm^{-1}), IR Intensities (km mol^{-1}), and Refined Energies (Hartree) for Neutral POM Molecules (H–(CH$_2$O)$_n$–H; $n = 2-4$)

Structure	Cartesian Coordinates			Vibrational Frequencies[a]		Energies (Hartree)
	Atom	X (Å)	Y (Å)	Z (Å)	(cm^{-1})		
a1	C	1.491044	−0.40501	0.105836	141.1076(2.6125)	187.8332(6.9343)	−229.9735877
	H	2.413952	−0.285602	−0.456963	360.1013(75.4013)	390.2328(49.9015)	
	H	1.696614	−0.242131	1.169934	585.3117(26.6653)	932.9411(31.4406)	...
	H	1.111769	−1.419873	−0.029097	1027.4807(146.6662)	1047.0658(104.4468)	...
	O	0.576214	0.564288	−0.387668	1139.1605(139.6082)	1176.0234(5.0116)	...
	C	−0.666482	0.550187	0.256406	1203.7620(25.8078)	1304.8840(17.9590)	...
	H	−0.547158	0.570856	1.344326	1385.9397(14.7368)	1434.0838(24.3675)	...
	H	−1.177358	1.454299	−0.082191	1476.6249(8.4696)	1486.9957(4.0660)	...
	O	−1.426854	−0.60614	−0.008759	1511.4052(5.7150)	1517.6650(1.6023)	...
	H	−1.640063	−0.613792	−0.948051	2990.5153(52.1183)	3006.9571(70.3915)	...
...	...	...	...	...	3057.7265(39.0012)	3059.3525(47.9857)	...
...	...	...	...	...	3118.7566(24.0425)	3799.6668(29.9923)	...
a2	C	1.477003	0.420577	0.082282	136.3993(6.8158)	187.6477(7.6166)	−229.9709847
	H	2.455416	0.191454	−0.333821	304.1224(76.4284)	391.5910(25.9102)	
	H	1.160916	1.399564	−0.291248	570.6672(6.8830)	935.3822(34.2416)	...
	H	1.558574	0.463773	1.176195	1023.7493(235.7588)	1051.0512(22.4212)	...
	O	0.597303	−0.609123	−0.326625	1126.7902(120.6891)	1174.4640(7.8643)	...
	C	−0.67493	−0.545772	0.255621	1208.3510(66.8894)	1310.3811(23.7198)	...
	H	−1.183789	−1.456288	−0.051417	1386.5295(14.9274)	1436.1370(15.5228)	...
	H	−0.581996	−0.514547	1.350937	1474.5842(4.5836)	1490.9860(2.1875)	...
	O	−1.465914	0.528425	−0.198383	1504.5729(0.9045)	1514.2799(7.0735)	...
	H	−1.272672	1.312797	0.322004	2949.4786(77.5608)	2971.6501(66.2138)	...
...	...	...	...	...	3028.0844(52.9477)	3111.4067(30.1805)	...
...	...	...	...	...	3114.6596(21.7911)	3829.4371(27.1110)	...
a3	C	−1.755793	0.042031	0.036501	101.3261(2.3308)	203.3508(4.0372)	−229.9700966
	H	−2.458692	−0.784486	−0.037475	291.7079(46.5070)	358.3398(79.2251)	
	H	−1.889821	0.537382	1.006303	527.0533(10.5103)	965.7258(65.7487)	...
	H	−1.977601	0.766689	−0.756144	1072.9943(83.8876)	1117.0211(87.2035)	...
	O	−0.457422	−0.498413	−0.098762	1131.2109(207.5847)	1178.2497(2.7361)	...
	C	0.555527	0.477697	0.01235	1224.8603(23.7135)	1257.2668(12.5809)	...
	H	0.507001	1.185965	−0.822422	1391.6141(22.6201)	1443.1740(48.8794)	...
	H	0.4213	1.027791	0.958265	1482.1054(12.7697)	1490.1552(6.6540)	...
	O	1.799363	−0.136306	−0.063409	1509.4899(5.8891)	1542.1824(0.7145)	...
	H	1.863884	−0.773957	0.65574	2917.2341(86.3546)	2970.8273(67.8086)	...
...	...	...	...	...	3008.4400(98.0596)	3011.4722(31.2865)	...
...	...	...	...	...	3115.4122(23.6876)	3801.0605(33.3060)	...
b1	C	1.932473	0.674372	−0.401849	96.4255(2.4311)	125.4053(4.7459)	−344.3699494
	H	2.474208	1.511723	0.031768	140.7093(4.3601)	191.7384(11.6392)	
	H	2.650158	−0.042032	−0.814376	329.8204(7.9797)	425.6186(28.9411)	...
	H	1.282061	1.032947	−1.201321	480.1036(29.6124)	514.0188(94.6403)	...
	O	1.178534	0.079864	0.652173	642.9436(10.8379)	911.9357(19.0547)	...
	C	0.486589	−1.083829	0.267212	935.3646(54.4800)	1014.6565(236.6190)	...
	H	1.151685	−1.774178	−0.258868	1081.8646(234.0922)	1083.6581(15.0442)	...
	H	0.131206	−1.529316	1.201431	1117.3758(107.7703)	1162.6810(96.9192)	...
	O	−0.58435	−0.844864	−0.607681	1178.8372(3.8447)	1232.2356(35.5632)	...
	C	−1.671818	−0.154039	−0.019489	1298.7063(21.0233)	1338.4686(3.1751)	...
	H	−2.520694	−0.300361	−0.682498	1400.4496(11.4080)	1429.6414(12.1605)	...
	H	−1.879361	−0.598094	0.964278	1452.5370(32.3866)	1475.7253(3.0755)	...
	O	−1.474285	1.228401	0.081071	1488.9982(4.9214)	1502.1870(1.4775)	...
	H	−0.731917	1.373082	0.679834	1512.7237(8.1095)	1519.5050(3.1023)	...
...	...	...	...	...	2957.3616(72.5861)	3000.3806(62.6884)	...
...	...	...	...	...	3005.7652(57.5167)	3054.6558(41.5670)	...
...	...	...	...	...	3070.5885(27.9393)	3115.4527(32.6774)	...
...	...	...	...	...	3121.7448(19.8596)	3777.6043(52.9355)	...
b2	C	2.385811	0.450983	−0.011837	67.9283(0.1019)	103.4832(2.0810)	−344.3693579
	H	2.917382	−0.122754	0.755763	145.1559(2.3985)	198.4990(9.7805)	
	H	3.086724	0.734054	−0.793725	272.9484(1.2797)	378.5384(134.7896)	...
	H	1.969876	1.351296	0.445487	425.2505(6.4372)	581.7574(14.1187)	...
	O	1.377196	−0.338906	−0.626574	606.4536(16.4201)	924.1797(6.4571)	...
	C	0.416298	−0.827464	0.262976	938.3915(64.5705)	998.0126(334.9991)	...
	H	−0.170202	−1.557885	−0.294299	1038.2157(214.6545)	1101.4503(78.7398)	...

Table A2
(Continued)

Structure	Cartesian Coordinates				Vibrational Frequencies[a]		Energies (Hartree)
	Atom	X (Å)	Y (Å)	Z (Å)	(cm^{-1})		
	H	0.885155	−1.291832	1.135476	1121.7975(82.7420)	1174.0987(75.9442)	...
	O	−0.421416	0.186093	0.790303	1176.3925(8.5920)	1232.9476(13.8150)	...
	C	−1.375784	0.681362	−0.126625	1291.9344(23.0842)	1335.2839(0.8999)	...
	H	−1.742029	1.608779	0.31781	1387.7241(12.9233)	1418.3567(17.6118)	...
	H	−0.919303	0.881182	−1.096305	1444.8213(11.2045)	1475.2746(0.9442)	...
	O	−2.417308	−0.229771	−0.372493	1487.8683(4.0374)	1509.8155(7.3142)	...
	H	−2.89333	−0.37145	0.452826	1516.0116(3.2195)	1526.1859(2.0709)	...
	...	...	...	...	2990.8963(51.4879)	3016.2330(80.0497)	...
	...	...	...	...	3034.8366(44.3942)	3056.2372(39.0271)	...
	...	...	...	...	3087.4285(9.1772)	3092.0397(37.2983)	...
	...	...	...	...	3118.6600(24.2950)	3799.4771(32.7526)	...
b3	C	−2.223775	0.395461	0.467371	59.6931(1.0620)	93.0328(2.5926)	−344.3663998
	H	−2.83253	1.282033	0.304774	127.3541(4.3218)	179.8631(3.5122)	
	H	−2.869103	−0.490428	0.445429	318.0405(29.0289)	351.9258(120.9282)	...
	H	−1.747121	0.45869	1.448649	403.5418(14.6252)	522.7964(19.4460)	...
	O	−1.265023	0.354165	−0.578728	615.9116(10.9035)	921.5918(25.4907)	...
	C	−0.446963	−0.776913	−0.548726	942.4871(28.4611)	1009.3797(266.2234)	...
	H	−1.052233	−1.680852	−0.420785	1051.4110(167.5458)	1112.8436(125.6434)	...
	H	0.080294	−0.798315	−1.503639	1124.9506(132.0950)	1175.5124(14.2402)	...
	O	0.473052	−0.773481	0.527868	1177.6548(88.8024)	1232.5935(11.3530)	...
	C	1.763334	−0.288598	0.227275	1285.6551(31.2200)	1340.2960(1.6821)	...
	H	2.330816	−0.42766	1.150727	1378.3685(18.7955)	1430.1523(13.0489)	...
	H	2.217663	−0.871185	−0.579159	1450.0941(20.8898)	1476.2753(4.4159)	...
	O	1.787767	1.039025	−0.219175	1488.3904(3.8317)	1501.8961(2.8972)	...
	H	1.35027	1.590349	0.438758	1513.3856(6.9830)	1525.9992(0.4696)	...
	...	...	...	...	2986.2527(45.0472)	2997.3450(79.6156)	...
	...	...	...	...	3012.4677(76.0496)	3049.0629(37.3888)	...
	...	...	...	...	3055.7294(45.0762)	3074.1627(35.2019)	...
	...	...	...	...	3116.6104(24.4665)	3799.4046(27.5867)	...
c1	C	−3.194751	0.035628	0.374179	50.3504(0.5299)	69.3674(1.2700)	−458.7654733
	H	−3.498878	1.079579	0.507664	101.5210(1.0819)	122.7286(2.3983)	
	H	−4.056863	−0.549942	0.064118	145.2076(3.1822)	206.3555(26.9300)	...
	H	−2.818589	−0.34804	1.324854	250.2051(2.8343)	398.2586(29.1568)	...
	O	−2.224141	−0.079924	−0.658616	420.1316(11.8926)	472.5419(46.1905)	...
	C	−1.065737	0.66374	−0.438416	510.3669(91.1011)	599.4120(4.2884)	...
	H	−0.506173	0.650935	−1.373024	644.7978(11.7541)	904.3762(5.1105)	...
	H	−1.301275	1.690064	−0.142285	934.5575(44.0193)	939.1905(61.9086)	...
	O	−0.269555	0.148549	0.622997	967.3146(496.3166)	1064.6221(234.0351)	...
	C	0.40705	−1.058	0.29885	1084.2382(11.5778)	1104.1175(41.2277)	...
	H	0.726702	−1.470823	1.259826	1120.3160(98.3437)	1151.3158(212.2370)	...
	H	−0.263154	−1.747146	−0.213669	1176.5280(6.1648)	1198.1860(16.8466)	...
	O	1.501464	−0.862881	−0.552019	1243.4872(37.9513)	1293.2504(23.9750)	...
	C	2.588315	−0.170009	0.037084	1327.2236(3.0956)	1342.7381(2.8213)	...
	H	2.757139	−0.575033	1.044646	1400.1479(13.0269)	1417.4486(11.6993)	...
	H	3.451375	−0.365392	−0.594112	1440.9035(3.0074)	1452.7494(32.0604)	...
	O	2.421784	1.219146	0.069701	1475.7077(1.0257)	1488.7069(4.4746)	...
	H	1.664041	1.408525	0.63529	1506.7780(2.7307)	1510.2757(6.5195)	...
	...	...	...	...	1516.6698(3.0219)	1522.8484(2.1140)	...
	...	...	...	...	2958.8488(73.3889)	2994.3235(49.3542)	...
	...	...	...	...	3017.5729(97.9790)	3021.1949(18.8836)	...
	...	...	...	...	3058.7569(36.6538)	3094.5456(12.0501)	...
	...	...	...	...	3099.2965(23.2324)	3116.2070(33.6374)	...
	...	...	...	...	3121.8406(22.7497)	3782.7251(55.9499)	...
c2	C	−1.71025	−1.206269	0.801434	39.1789(6.4616)	82.9647(5.3255)	−458.7631172
	H	−2.535852	−0.827483	1.41108	124.9391(3.2367)	132.5434(0.9339)	
	H	−1.89181	−2.253259	0.572058	149.1383(4.6512)	169.8797(6.3083)	...
	H	−0.77001	−1.115348	1.344757	315.2992(1.1269)	407.4609(4.6685)	...
	O	−1.660466	−0.52123	−0.452024	426.9949(7.9011)	449.7130(43.1560)	...
	C	−1.505093	0.868391	−0.390663	519.5332(42.7812)	533.6064(95.3850)	...
	H	−2.096756	1.287487	−1.202628	616.9327(10.6583)	895.3123(10.2142)	...
	H	−1.849724	1.256967	0.57597	920.6532(32.3249)	937.5940(88.8519)	...
	O	−0.182528	1.304103	−0.641801	991.0720(216.0945)	1077.5280(114.7057)	...

Table A2
(Continued)

Structure	Cartesian Coordinates				Vibrational Frequencies[a]		Energies (Hartree)
	Atom	X (Å)	Y (Å)	Z (Å)	(cm^{-1})		
	C	0.700142	1.428571	0.450738	1088.0706(233.4311)	1102.5314(32.9389)	...
	H	1.487378	2.098718	0.095772	1111.7139(179.9050)	1169.1243(88.6663)	...
	H	0.19211	1.862407	1.31595	1180.0697(5.4494)	1195.2672(70.0857)	...
	O	1.249007	0.217846	0.897261	1242.2996(32.6669)	1293.9960(34.2993)	...
	C	1.982038	−0.502645	−0.09048	1324.7792(6.8359)	1345.1559(6.0797)	...
	H	2.391539	0.212615	−0.814711	1397.1934(10.9074)	1430.1031(3.4232)	...
	H	2.790864	−1.011925	0.429275	1443.7875(13.0838)	1455.1086(25.8053)	...
	O	1.223729	−1.494788	−0.709179	1479.0436(4.7916)	1493.2549(2.9711)	...
	H	0.443299	−1.085909	−1.107762	1501.0861(3.3057)	1509.5263(7.4624)	...
	...	...	...	...	1513.9747(3.1303)	1522.9614(0.5391)	...
	...	...	...	...	2977.6020(65.5818)	2979.1102(40.5971)	...
	...	...	...	...	3007.8333(70.4848)	3013.5517(70.4167)	...
	...	...	...	...	3061.5323(41.4074)	3087.9123(21.9924)	...
	...	...	...	...	3095.1563(30.3754)	3101.6257(37.3413)	...
	...	...	...	...	3129.7675(13.5728)	3741.1443(102.5792)	...
c3	C	3.175324	0.071732	0.171183	30.9190(0.4071)	70.2410(2.3712)	−458.7615039
	H	2.993202	1.102368	−0.14129	86.0155(0.2800)	125.7460(1.8192)	
	H	3.855303	0.066853	1.020017	139.5632(2.6590)	190.2434(12.4282)	...
	H	3.635981	−0.47305	−0.660515	279.9099(2.6024)	352.6217(111.2175)	...
	O	1.979318	−0.56757	0.594611	394.8893(9.3704)	437.1996(6.6670)	...
	C	1.010302	−0.687103	−0.407343	489.6331(36.8764)	571.8371(22.9446)	...
	H	1.442366	−1.095498	−1.32584	621.2788(18.7308)	919.1629(50.4784)	...
	H	0.242908	−1.352621	−0.015854	934.5252(65.4132)	942.4729(26.3782)	...
	O	0.455233	0.558197	−0.794685	989.5682(439.6260)	1030.2252(51.8755)	...
	C	−0.397575	1.174692	0.138735	1050.4502(216.8767)	1115.1980(56.4615)	...
	H	−0.165763	0.836351	1.154133	1132.3617(159.0196)	1164.5623(76.8862)	...
	H	−0.226452	2.245405	0.048267	1176.3753(6.8422)	1196.9224(91.9290)	...
	O	−1.771045	0.988937	−0.137408	1245.3787(27.3167)	1289.2031(22.0866)	...
	C	−2.421728	−0.082945	0.492326	1326.0609(2.2953)	1349.4525(6.8826)	...
	H	−2.108444	−0.174111	1.5357	1384.0529(18.5084)	1423.2726(1.8424)	...
	H	−3.485393	0.158205	0.439777	1440.7015(12.7898)	1452.2155(15.4175)	...
	O	−2.155929	−1.337692	−0.089371	1475.7334(0.5456)	1487.7897(4.2356)	...
	H	−2.442266	−1.307125	−1.008971	1504.1766(1.3557)	1511.0318(7.1459)	...
	...	...	...	...	1519.2759(2.3176)	1527.7535(1.2457)	...
	...	...	...	...	2991.5870(51.8688)	3006.1949(37.5929)	...
	...	...	...	...	3015.9808(81.9295)	3018.9171(43.4603)	...
	...	...	...	...	3055.0118(38.2633)	3066.0863(43.6227)	...
	...	...	...	...	3100.8119(27.7258)	3107.1715(11.7901)	...
	...	...	...	...	3117.4428(26.2593)	3797.4760(36.5608)	...

Note.
[a] IR intensities are in parentheses (km mol^{-1}).

carry out high-level single-point energy calculations. The energies were subsequently refined by extrapolation to the complete basis set (CBS) limit using a two-point formula at the CCSD(T) level (S. B. Huh & J. S. Lee 2003), followed by correction for the zero-point vibrational energy (ZPVE) as calculated at the B3LYP/cc-pVTZ level of theory. Optimized Cartesian coordinates, vibrational frequencies, and refined energies are compiled in Table A2. The accuracy for the final energy is within 5 kJ mol^{-1}, and the ionization energy is determined by the difference in energy between the neutral molecule and its corresponding cation states. Consequently, the calculated ionization energies at this level of theory are typically accurate within 0.1 eV from the experimental results (C. Zhu et al. 2019). For potential energy surfaces, the transition state of cations was verified by intrinsic reaction coordinate calculations, and the relative energies were then obtained at the same level of theory. All computations involving B3LYP and CCSD(T) methods were performed utilizing the Gaussian16 program package (M. J. Frisch et al. 2016).

ORCID iDs

Jiuzhong Yang https://orcid.org/0000-0002-7076-3412
Ralf I. Kaiser https://orcid.org/0000-0002-7233-7206
Tao Yang https://orcid.org/0000-0003-4101-2385

References

Abplanalp, M. J., Gozem, S., Krylov, A. I., et al. 2016, PNAS, 113, 7727
Altwegg, K., Balsiger, H., Bar-Nun, A., et al. 2016, SciA, 2, e1600285
Altwegg, K., Balsiger, H., Berthelier, J. J., et al. 2017, MNRAS, 469, S130
Arumainayagam, C. R., Garrod, R. T., Boyer, M. C., et al. 2019, ChSRv, 48, 2293
Bartlett, R. J., & Musiał, M. 2007, RvMP, 79, 291

Becke, A. D. 1993, JChPh, 98, 5648
Bennett, C. J., Chen, S.-H., Sun, B.-J., Chang, A. H. H., & Kaiser, R. I. 2007, ApJ, 660, 1588
Bennett, C. J., & Kaiser, R. I. 2007, ApJ, 661, 899
Bockelée-Morvan, D., & Biver, N. 2017, RSPTA, 375, 20160252
Bossa, J. B., Isokoski, K., de Valois, M. S., & Linnartz, H. 2012, A&A, 545, A82
Bouilloud, M., Fray, N., Bénilan, Y., et al. 2015, MNRAS, 451, 2145
Butscher, T., Duvernay, F., Danger, G., & Chiavassa, T. 2016, A&A, 593, A60
Butscher, T., Duvernay, F., Danger, G., et al. 2019, MNRAS, 486, 1953
Butscher, T., Duvernay, F., Rimola, A., Segado-Centellas, M., & Chiavassa, T. 2017, PCCP, 19, 2857
Cernicharo, J., Marcelino, N., Roueff, E., et al. 2012, ApJL, 759, L43
Chuang, K. J., Fedoseev, G., Ioppolo, S., Van Dishoeck, E. F., & Linnartz, H. 2016, MNRAS, 455, 1702
Cody, G. D., Heying, E., Alexander, C. M. O., et al. 2011, PNAS, 108, 19171
Cordiner, M. A., Remijan, A. J., Boissier, J., et al. 2014, ApJL, 792, L2
Cottin, H., Bénilan, Y., Gazeau, M.-C., & Raulin, F. 2004, Icar, 167, 397
Cottin, H., Gazeau, M. C., Benilan, Y., & Raulin, F. 2001, ApJ, 556, 417
DiSanti, M. A., Bonev, B. P., Magee-Sauer, K., et al. 2006, ApJ, 650, 470
Drouin, D., Couture, A. R., Joly, D., et al. 2007, Scanning, 29, 92
Dunning, T. H., Jr. 1989, JChPh, 90, 1007
Duvernay, F., Danger, G., Theulé, P., Chiavassa, T., & Rimola, A. 2014, ApJ, 791, 75
Ejeta, C., Gibb, E., Roth, N., et al. 2023, AJ, 167, 32
Förstel, M., Tsegaw, Y. A., Maksyutenko, P., et al. 2016, ChPhC, 17, 2726
Francisco, J. S., Goldstein, A. N., & Williams, I. H. 1988, JChPh, 89, 3044
Fray, N., Bénilan, Y., Biver, N., et al. 2006, Icar, 184, 239
Frisch, M. J., Trucks, G. W., Schlegel, H. B., et al. 2016, Gaussian 2016 (Revision B.01) (Wallingford, CT: Gaussian, Inc.)
Goesmann, F., Rosenbauer, H., Bredehöft, J. H., et al. 2015, Sci, 349, aab0689
Hänni, N., Altwegg, K., Baklouti, D., et al. 2023, A&A, 678, A22
Hänni, N., Altwegg, K., Combi, M., et al. 2022, NatCo, 13, 3639
Hansen, N. A., Price, T. D., Filardi, L. R., et al. 2024, JChPh, 160, 124306
Harris, T. D., Lee, D. H., Blumberg, M. Q., & Arumainayagam, C. R. 1995, JPhCh, 99, 9530
He, J., Simons, M., Fedoseev, G., et al. 2022, A&A, 659, A65
Huebner, W. F., Boice, D. C., & Korth, A. 1989, AdSpR, 9, 29
Huebner, W. F. 1987, Sci, 237, 628
Huh, S. B., & Lee, J. S. 2003, JChPh, 118, 3035
Iwasaki, M., & Toriyama, K. 1978, JAChS, 100, 1964
Johnson, R. A., & Stanley, A. E. 1991, ApSpe, 45, 218
Jones, B. M., & Kaiser, R. I. 2013, JPCL, 4, 1965
Kendall, R. A., Dunning, T. H., Jr., & Harrison, R. J. 1992, JChPh, 96, 6796
Kleimeier, N. F., Eckhardt, A. K., & Kaiser, R. I. 2021, JAChS, 143, 14009
Komorek, R., Xu, B., Yao, J., et al. 2018, RScI, 89, 115105
Kostko, O., Bandyopadhyay, B., & Ahmed, M. 2016, ARPC, 67, 19
Krishna Swamy, K. S., Sandford, S. A., Allamandola, L. J., Witteborn, F. C., & Bregman, J. D. 1989, ApJ, 340, 537
Layssac, Y., Gutiérrez-Quintanilla, A., Chiavassa, T., & Duvernay, F. 2020, MNRAS, 496, 5292
Lee, C., Yang, W., & Parr, R. G. 1988, PhRvB, 37, 785
Leseigneur, G., Bredehöft, J. H., Gautier, T., et al. 2022, ACIE, 61, e202201925
Li, Y., & Qi, F. 2010, Acc. Chem. Res., 43, 68
Maity, S., Kaiser, R. I., & Jones, B. M. 2015, PCCP, 17, 3081
Marks, J. H., Bai, X., Nikolayev, A. A., et al. 2024, JAChS, 146, 12174
McGuire, B. A., Shingledecker, C. N., Willis, E. R., et al. 2017, ApJL, 851, L46
Meringer, M., Giri, C., & Cleaves, H. J., II. 2018, ESC, 2, 1256
Missaoui, D., Brahem, S., Najar, F., Yazidi, O., & Senent, M. L. 2024, ESC, 8, 1236
Motiyenko, R. A., Margulès, L., Despois, D., & Guillemin, J. C. 2018, PCCP, 20, 5509
Noble, J. A., Theule, P., Mispelaer, F., et al. 2012, A&A, 543, A5
Purvis, G. D., III., & Bartlett, R. J. 1982, JChPh, 76, 1910
Qi, F. 2013, PComI, 34, 33
Rivilla, V. M., Beltrán, M. T., Cesaroni, R., et al. 2017, A&A, 598, A59
Rubin, M., Altwegg, K., Balsiger, H., et al. 2015, Sci, 348, 232
Schmidt, F., Swiderek, P., & Bredehöft, J. H. 2021, ESC, 5, 391
Schneider, H., Caldwell-Overdier, A., Coppieters't Wallant, S., et al. 2019, MNRAS, 485, L19
Schutte, W. A., Allamandola, L. J., & Sandford, S. A. 1993, Sci, 259, 1143
Senevirathne, B., Andersson, S., Dulieu, F., & Nyman, G. 2017, MolAs, 6, 59
Sullivan, K. K., Boamah, M. D., Shulenberger, K. E., et al. 2016, MNRAS, 460, 664
Tachikawa, H. 1993, CPL, 212, 27
Toriyama, K., & Iwasaki, M. 1979, JAChS, 101, 2516
Turner, A. M., Abplanalp, M. J., Chen, S. Y., et al. 2015, PCCP, 17, 27281
Turner, A. M., Bergantini, A., Koutsogiannis, A. S., et al. 2021, ApJ, 916, 74
Turner, A. M., & Kaiser, R. I. 2020, Acc. Chem. Res., 53, 2791
Vanysek, V., & Wickramasinghe, N. C. 1999, Ap&SS, 268, 115
Wang, H., Guan, J., Gao, J., et al. 2022, PCCP, 24, 26915
Wang, J., Nikolayev, A. A., Marks, J. H., et al. 2023, JPCL, 14, 6078
Watanabe, N., Nagaoka, A., Shiraki, T., & Kouchi, A. 2004, ApJ, 616, 638
Wright, I. P., Sheridan, S., Barber, S. J., et al. 2015, Sci, 349, aab0673
Zhou, Z., Yang, J., Yuan, W., et al. 2022, PCCP, 24, 21567
Zhu, C., Frigge, R., Bergantini, A., Fortenberry, R. C., & Kaiser, R. I. 2019, ApJ, 881, 156
Zhu, C., Wang, H., Medvedkov, I., et al. 2022, JPCL, 13, 6875